Magnetic Response of *Magnetospirillum gryphiswaldense* observed inside a microfluidic channel

M. P. Pichel[a,b], T. A. G. Hageman[a,b], I. S. M. Khalil[c], A. Manz[a], L. Abelmann[a,b,1],

[a] *KIST Europe, Saarbrücken, Germany*
[b] *University of Twente, The Netherlands*
[c] *The German University in Cairo, New Cairo City, Egypt*

Abstract

In this study we modelled and measured the U-turn trajectories of individual magnetotactic bacteria under the application of rotating magnetic fields, ranging in amplitude from 1 to 12 mT. The model is based on the balance between rotational drag and magnetic torque. For accurate verification of this model, bacteria were observed inside 5 µm tall microfluidic channels, so that they remained in focus during the entire trajectory. From the analysis of hundreds of trajectories and accurate measurements of bacteria and magnetosome chain dimensions, we confirmed that the model is correct within measurement error. The resulting average rate of rotation of *Magnetospirillum gryphiswaldense* is 0.74 ± 0.03 rad/mTs.

Keywords: Rotational magnetic torque, rotational drag torque, magnetotactic bacteria, microfluidic, control

1. Introduction

Magnetotactic bacteria [1] (MTB[1]) possess an internal chain of magnetosome vesicles [2] which biomineralise nanometer sized magnetic crystals (Fe_3O_4 or Fe_3S_4 [3, 4, 5]), encompassed by a membrane (magnetosome) [6]. This magnetosome chain (MC) acts much like a compass needle. The magnetic torque acting on the MC aligns the bacteria with the earth magnetic field [7]. This is a form of magnetoreception [8], working in conjunction with aero-taxis [9]. At high latitudes the earth's magnetic field is not only aligned North-South, but also substantially inclined with respect to the earth's surface [10]. The MTB are therefore aligned vertically, which converts a three-dimensional search for the optimal (oxygen) conditions into a more efficient one-dimensional search [11] (gravitational forces do not play a significant role at the scale of a bacterium). This gives MTB an evolutionary advantage over non-magnetic bacteria in environments with stationary chemical gradients more or less perpendicular to the water surface.

In this paper we address the question of how the MTB of type *Magnetosprilillum gryphiswaldense* (MSR-1) respond to varying magnitudes of the external field, in particular a field that is rotating. Even though the response of individual magneto-tactic bacteria to an external magnetic field has been modelled and observed [12, 13, 14, 7, 15], there has been no thorough observation of the dependence on the field strength. The existing models predict a linear relation between the angular velocity of the bacterium and the field strength, but this has not been confirmed experimentally. Nor has there been an analysis of the spread in response over the population of bacteria. The main reason for the absence of experimental data is that the depth of focus at the magnification required prohibits the observation of multiple bacteria in parallel. In this paper, we introduce microfluidic chips with a channel depth of only 5 µm, which ensures that all bacteria in the field of view remain in focus.

The second motivation for studying the response of MTB to external magnetic fields, is that they are an ideal model system for self propelled medical microrobotics [16, 17]. Medical microrobotics is a novel form of minimally invasive surgery (MIS), in which one tries to reduce the patient's surgical trauma while enabling clinicians to reach deep seated locations within the human body [18, 19, 20].

The current approach in medical microrobotics is to insert the miniaturized tools needed for a medical procedure into the patient through a small insertion or orifice. By reducing the size of these tools a larger range of natural pathways becomes available. Currently, these tools are mechanically connected to the outside world. If this connection can be removed, so that the tools become untethered, (autonomous) manoeuvring through the veins and arteries of the body becomes possible [21].

If the size and/or application of these untethered systems inside the human body prohibits the storage of energy for propulsion, the energy has to be harvested from the environment. One solution is the use of alternating magnetic fields [17]. This method is simple, but although impressive progress has been made, it is appallingly ineffi-

*Corresponding author
Email address: l.abelmann@kist-europe.de (L. Abelmann)

[1] Throughout this paper we will use the acronym MTB to indicate the single bacterium as well as multiple bacteria

cient. Only a fraction, 10^{-12}, of the supplied energy field is actually used by the microrobot. This is not a problem for microscopy experiments, but will become a serious issue if the microrobots are to be controlled deep inside the human body. The efficiency would increase dramatically if the microrobot could harvest its energy from the surrounding liquid. In human blood, energy is abundant and used by all cells for respiration.

For self-propelled objects, only the direction of motion needs to be controlled by the external magnetic field. There is no need for field gradients to apply forces, so the field is allowed to be weaker and uniform when solely using magnetic torque [22]. Compared to systems that derive their energy for propulsion from the magnetic field, the field can be small in magnitude and only needs to vary slowly. As a result, the energy requirements are low and overheating problems can be avoided.

MTB provide a perfect biokleptic model to test concepts and study the behaviour of self-propelled micro-objects steered by external magnetic fields [23]. The direction of the motion of an MTB is modified by the application of a magnetic field at an angle with the easy axis of magnetization of the magnetosome. The resulting magnetic torque causes a rotation of the MTB at a speed that is determined by the balance between the magnetic torque and the rotational drag torque. Under the application of a uniform rotating field, the bacteria follow U-turn trajectories [12, 24, 25].

The magnetic torque is often modelled by assuming that the magnetic element is a permanent magnet with dipole moment $\boldsymbol{m}$ [Am^2] on which the magnetic field $\boldsymbol{B}$ [T] exerts a torque $\boldsymbol{\Gamma} = \boldsymbol{m} \times \boldsymbol{B}$ [Nm]. This simple model suggest that the torque increases linearly with the field strength, where it is assumed that the atomic dipoles are rigidly fixed to the lattice, and hardly rotate at all. This is usually only the case for very small magnetic fields.

In general one should consider a change in the magnetic energy as a function of the magnetization direction with respect to the object (magnetic anisotropy). This is correctly suggested by Erglis *et al.* for magnetotactic bacteria [7]. An estimation of the magnetic dipole moment can be obtained by studying the dynamics of MTB [13].

Recent studies of the dynamics of MTB in a rotating magnetic field show that a random walk is still present regardless of the presence of a rotating field [26, 15]. The formation and control of aggregates of MTB in both two- and three-dimensional control systems has been achieved *in vitro* [27, 28, 29] as well as *in vivo* [20], showing that MTB can use the natural hypoxic state surrounding cancerous tissue for targeted drug delivery.

Despite these impressive results, successful control of individual MTB is much less reported. This is because many experiments suffer from a limited depth of focus of the microscope system, leading to a loss of tracking. A collateral problem is overheating of the electromagnets in experiments that take longer than a few minutes. We recently demonstrated the effect of varying field strengths on the control of magneto-tactic bacteria [30]. In the present paper we provide the theoretical framework and systematically analyse the influence of the magnetic field on the trajectories of individual MTB. This knowledge will contribute to more efficient control of individual MTB, and ultimately self-propelled robotic systems in general.

We present a thorough theoretical analysis of the magnetic and drag torques on MTB. This model is used to derive values for the proportionality between the average rate of rotation and the magnetic field during a U-turn trajectory under a magnetic field reversal. The theory is used to predict U-turn trajectories of MTB, which are the basis for our experimental procedures.

Lastly, we present statistically significant experimental results which verify our theoretical approach and employ a realistic range of magnetic field strength and rotational speed of the applied magnetic field to minimize energy input.

2. Theory

2.1. The Rate of Rotation

2.1.1. The dependence on the field

The magnetic torque Γ [Nm] is equal to the change in total magnetic energy U [J] with changing applied field angle. We consider only the demagnetization and external field energy terms. The demagnetization energy is caused by the magnetic stray field $\boldsymbol{H}_\mathrm{d}$ [A/m] that arises due to the magnetosome magnetization $\boldsymbol{M}$ [A/m]. In principle, one has to integrate the stray field over all space. Fortunately, this integral is mathematically equivalent to [31]

$$U_\mathrm{d} = \tfrac{1}{2}\mu_0 \int \boldsymbol{M} \cdot \boldsymbol{H}_\mathrm{d} \mathrm{d}V, \tag{1}$$

with μ_o the vacuum permeability, $4\pi 10^{-7}$. In this formulation, the integral is conveniently restricted to the volume V of the magnetic material.

The demagnetization energy acts to orient the magnetization so that the external stray field energy is minimized. We can define a shape anisotropy term K [J/m^3] to represent the energy difference between the hard and easy axes of magnetization, which are perpendicular to each other,

$$K = \left(U_{\mathrm{d,\ max}} - U_{\mathrm{d,\ min}}\right)/V. \tag{2}$$

The external field energy is caused by the externally applied field $\boldsymbol{H}$ [A/m]

$$U_\mathrm{H} = -\mu_0 \int \boldsymbol{M} \cdot \boldsymbol{H} \mathrm{d}V, \tag{3}$$

and acts to align $\boldsymbol{M}$ parallel to $\boldsymbol{H}$. Assuming that the magnetic element of volume V is uniformly magnetized with saturation magnetization M_s [A/m], the total energy can then be expressed as

$$U = KV sin^2(\theta) - \mu_0 M_\mathrm{s} H V cos(\varphi - \theta). \tag{4}$$

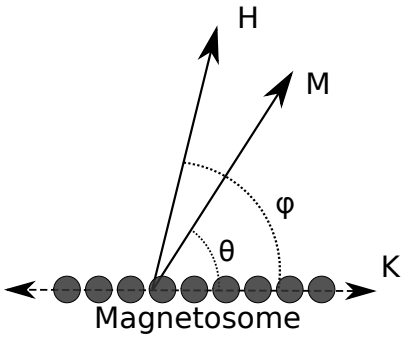

Figure 1: Definition of the field angle φ and the magnetization angle θ between the easy axis K, the magnetization M and the magnetic field H.

The angles θ and φ are defined as in figure 1. Normalizing the energy, field, and torque by

$$u = {}^{U}/_{KV} \tag{5}$$
$$h = {}^{\mu_0 HM}/_{2K} \tag{6}$$
$$\tau = {}^{\Gamma}/_{KV}, \tag{7}$$

respectively, the expression for the energy can be simplified to

$$u = \sin^2(\theta) - 2h\cos(\varphi - \theta). \tag{8}$$

The equilibrium magnetization direction is reached for ${}^{\partial u}/_{\partial\theta} = 0$. The solution for this relationship cannot be expressed in an analytically concise form. The main results are however that for $h < {}^{1}/_{\sqrt{2}}$, the maximum torque is reached at the field angle $\varphi_{\max} = {}^{\pi}/_{2}$,

$$\tau_{\max} = 2h\sqrt{1-h^2} \qquad \text{for } h \leq {}^{1}/_{\sqrt{2}} \tag{9}$$
$$= 1 \qquad \text{for } h > {}^{1}/_{\sqrt{2}}. \tag{10}$$

The angle of magnetization at maximum torque can be approximated by

$$\theta_{\max} = h + 0.1h^2 \text{ for } h < {}^{1}/_{\sqrt{2}}, \tag{11}$$

where the error is smaller than 5×10^{-3} rad (1.6°) for $h < 0.5$.

For $h > 1$, the field angle $\varphi_{\max}$ at which the maximum torque is reached is smaller than ${}^{\pi}/_{2}$ and approaches ${}^{\pi}/_{4}$ for $h \to \infty$. This behaviour can be very well approximated by

$$\varphi_{\max} = \frac{\pi}{4}\left(1 + \frac{2}{3h}\right) \text{ for } h > 1, \tag{12}$$

where the error is smaller than $3 \times 10^{-3}\pi$ (0.5°).

In summary, and returning to variables with units, the maximum torque is $\Gamma_{\max} = KV$, which is reached at

$$H > \frac{\sqrt{2}K}{\mu_0 M_{\mathrm{s}}} \tag{13}$$

at an angle $\varphi = {}^{\pi}/_{2}$, which, to a good approximation, decreases linearly with $1/H$ to $\varphi = {}^{\pi}/_{4}$ at an infinite external field.

2.1.2. Demagnetization factor

The magnetization M_{s} is a material parameter, so the only variable to be determined is the magnetosome's demagnetization factor. As a first approximation, we can consider the chain of magnetic crystals in the magnetosome as a chain of n dipoles separated at a distance a, each with a dipole moment $m{=}M_s V$ [Am^2], where V is the volume of each single sphere. We assume that all dipoles are aligned parallel to the field ($\varphi = \theta$) to obtain an upper limit on the torque. (See figure 1 for the definition of the angles). The magnetic energy for such a dipole chain has been derived by Jacobs and Bean [32], which, rewritten in SI units, is

$$U = \frac{\mu_0 m^2}{4\pi a^3} n K_n \left(1 - 3\cos^2(\theta)\right) + \mu_0 n m H cos(\varphi - \theta) \tag{14}$$
$$K_n = \sum_{j=1}^{n} \frac{(n-j)}{nj^3}. \tag{15}$$

The maximum torque equals the energy difference between the state where all moments are parallel to the chain ($\theta{=}0$) and the state where they are perpendicular to the chain ($\theta{=}\pi/2$), under the condition that the angle between the moments and the field is zero:

$$\Gamma_{\max} = \frac{3\mu_0 m^2}{4\pi a^3} n K_n. \tag{16}$$

For a single dipole $n = 1$, $K_n{=}0$ and there is no energy difference, as expected.

Combined with equations (6) and (9), and reintroducing units, the field dependent torque becomes

$$\Gamma = \Gamma_{\max} 2h\sqrt{1-h^2} \text{ with} \tag{17}$$
$$h = \frac{H}{\Delta N M_{\mathrm{s}}}. \tag{18}$$

The magnetosome does not consist of point dipoles but should be approximated by spheres with radius r, spaced at a distance of a from each other (figure 2). We can modify the Jacob and Bean model by introducing the volume of a single sphere V and the magnetization M_s of the magnetite crystal (4.8×10^5 A/m [33]),

$$\Gamma_{\max} = \frac{1}{2}\mu_0 M_s^2 n V \Delta N \tag{19}$$
$$\Delta N = 2K_n \left(\frac{r}{a}\right)^3, \tag{20}$$

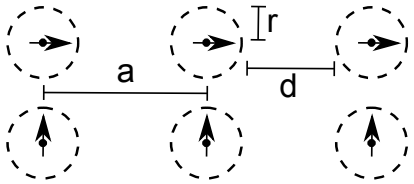

Figure 2: Chain of magnetic spheres of radius r, spaced at a distance d, approximated by point dipoles spaced by a distance $a = r + d$, magnetized along the longitudinal axis of the chain (top) or perpendicular to its longitudinal axis (bottom).

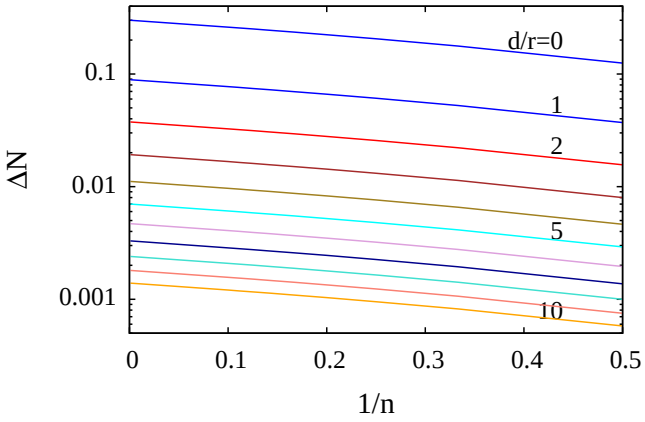

Figure 3: Difference in demagnetization factors of a chain of spheres as function of number of spheres n for varying spacing between the spheres d/r.

as a correction to equation 16. This correction is based on the fact that the field of a uniformly magnetized sphere is identical to a dipole field [34] outside the sphere, and the average of the magnetic field over a sphere not containing currents is identical to the field at the center of that sphere [35, 36].

For an infinitely long chain of touching spheres, d=0 and $n \to \infty$, the difference in demagnetization factors (ΔN) approaches 0.3 (Figure 3). Approximating the chain by a long cylinder (ΔN=0.5) [37, 7] therefore overestimates the maximum torque by 40%. Simply taking the total magnetic moment to calculate the torque, as if ΔN=1, would overestimate it by a factor of three.

2.1.3. Low field approximation

For low values of the field ($h \ll 1$), equation (16) can be approximated by

$$\Gamma \approx \Gamma_{\max} 2h = \mu_0 M_s n V H = mB, \qquad (21)$$

where m [Am^2] is the total magnetic moment of the magnetosome chain and assuming the permeability of the medium to be equal to vacuum. This approximation is commonly used in the field of MTB studies. Based on the

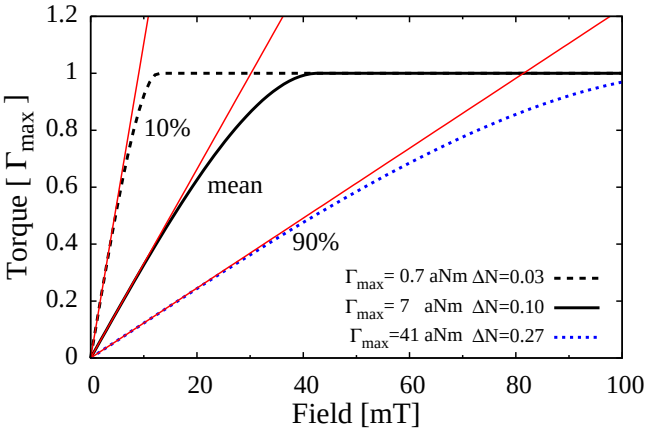

Figure 4: Magnetic torque on magnetotactic bacteria, normalized to the maximum torque, as a function of applied field for the average of the population, as well as the 10 % and 90 % cut-off (see table 1). The red solid asymptotes show the linear approximation for $\Gamma = mB$.

theory presented here, it is now possible to estimate up to which field value this is approximation is valid.

The normalization to the reduced field h is solely dependent on the magnetization and demagnetization factors of the chain. Based on the values for magnetosome morphology (table 1), we can estimate the field dependence of the torque. Figure 4 shows the torque as a function of the field for the range of values tabulated, normalized to the maximum torque. Also shown is the approximation for the case when the magnetization remains aligned with the easy axes. For *Magnetospirillum Gryphiswaldense*, the linear range is valid up to fields of about 10 mT for 90 % of the population.

2.1.4. Drag torque

Magnetotactic bacteria are very small, and rotate at a few revolutions per second only. Inertial forces therefore do not play a significant role. The ratio between the viscous and inertial forces is characterized by the Reynolds number Re, which for rotation at an angular velocity of ω [rad/s] is

$$Re = \frac{L^2 \rho \omega}{4\eta}, \qquad (22)$$

where L is the characteristic length (in our case, the length of the bacterium), ρ the density, and η the dynamic viscosity of the liquid (for water, these are, respectively, 10^3 kg/m^3, and 1 mPas). Experiments by Dennis *et al.* [38] show that a Stokes flow approximation for the drag torque is accurate up to Re=10. In experiments with bacteria, the Reynolds number is on the order of 10^{-3} and the Stokes flow approximation is certainly allowed. The drag torque is therefore simply given by

$$\Gamma_D = f_b \omega, \qquad (23)$$

The rotational drag coefficient of the bacterium, f_b, needs to be estimated for the type of MTB studied. In a first approximation, one could consider the MTB to be a rod of length L and diameter W. Unfortunately, there is no simple expression for the rotational drag of a cylinder. Dote [39] gives a numerical estimate of the rotational drag of a cylinder with spherical caps (spherocylinder). Fortunately, for typical MSR-1 dimensions, it can be shown that a prolate spheroid of equal length and diameter has a rotational drag coefficient that is within 10 % of that value. To a first approximation, one can therefore assume the rotational drag of an MSR-1 to be given by [40]

$$f_\mathrm{e} = \frac{\pi\eta L^3}{3\ln\left(\frac{2L}{W}\right) - \frac{3}{2}}. \tag{24}$$

However, the MSR-1 has a spiral shape, so the actual drag will be higher. Rather than resorting to complex finite element simulations, we chose to empirically determine the rotational drag torque by macroscopic experiments with 3D printed bacteria models in a highly viscous medium (Section 3.4.). We introduce a bacteria shape correction factor α_bs to the spheroid approximation, which is independent of the ratio L/W over the range of typical values for MSR-1 and has a value of about 1.65. The corrected rotational drag coeffient for the bacteria then becomes

$$f_\mathrm{b} = \alpha_\mathrm{bs} f_\mathrm{e}. \tag{25}$$

2.1.5. Diameter and duration of the U-turn

At the steady-state rate, the magnetic torque is balanced by the rotational drag torque, leading to a rate of rotation of

$$\omega = \frac{\Gamma}{f_\mathrm{b}} \approx \frac{mB\sin\phi(t)}{f_\mathrm{b}}. \tag{26}$$

The approximation is for low field values (see figure 4), in which case ϕ is the angle between the applied field and the long axis of the bacteria (magnetosome).

The maximum rate of rotation, mB/f_b, is obtained when the field is perpendicular to the long axis of the bacteria. Suppose that we construct a control loop to realize this condition over the entire period of a U-turn. Then the minimum diameter and duration of this loop would be

$$D_\mathrm{min} = \frac{2f_\mathrm{b}v}{mB} \tag{27}$$

$$T_\mathrm{min} = \frac{\pi f_\mathrm{b}}{mB}, \tag{28}$$

where D_min is the minimum size of a U-turn's diameter and T_min is the minimum time of a U-turn. On the other hand, if we reverse the field instantaneously, the torque will vary over the trajectory of the U-turn. Compared to the situation above, the diameter of the U-turn increases by a factor of $\pi/2$:

$$D = \frac{\pi f_\mathrm{b} v}{mB}. \tag{29}$$

The diameter of the U-turn increases with the velocity of the bacterium. To obtain a description that only depends on the dimensions of the bacteria, we introduce a new parameter v/D [rad/s], which can be interpreted as an average rate of rotation. The relation between the average rate of rotation and the magnetic field B is

$$\frac{v}{D} = \gamma B, \tag{30}$$

where the proportionality factor γ [rad/Ts] can be linked to the bacterial magnetic moment m and drag coefficient f_b [Nms],

$$\gamma = \frac{m}{\pi f_\mathrm{b}}. \tag{31}$$

Note, however, that this expression is only valid in the low field approximation.

The determination of the duration of the U-turn trajectory is complicated by the fact that the magnetic torque starts and ends at zero (at θ=0 or π). In this theoretical situation, the bacteria would never turn at all. Esquivel *et al.* [11] solve this problem by assuming a disturbance acting on the motion of the bacteria. This disturbance could be due to Brownian motion, as used by Esquivel *et al.*, or due to flagellar propulsion, as we use in the simulations in the following section. Assuming an initial disturbing angle of θ_i, the duration T [s] of the U-turn becomes

$$T = \frac{2f_\mathrm{b}}{mB}\ln\frac{2}{\theta_\mathrm{i}}. \tag{32}$$

2.2. U-turn Trajectory Simulations

To check the validity of the analytical approach, we performed simulations. The MTB are approximated by rigid magnetic dipoles with constant lateral velocity v at an orientation of $\theta_x(t)$ and angular velocity of $\omega(t)$ (see figure 5). They are subject to a magnetic field with magnitude B at an orientation of $\varphi_x(t)$, resulting in a magnetic torque of $\Gamma(t)$. In contrast to the analytical model, it is assumed that flagellar motion causes an additive sinusoidal torque $\Gamma_\mathrm{f}(t)$ with amplitude A_f and angular velocity ω_f. These should be in balance with the drag torque: $\Gamma_\mathrm{D} = f_\mathrm{b}\omega(t)$. The following set of equations link the physical model to the coordinates $x(t)$, $y(t)$:

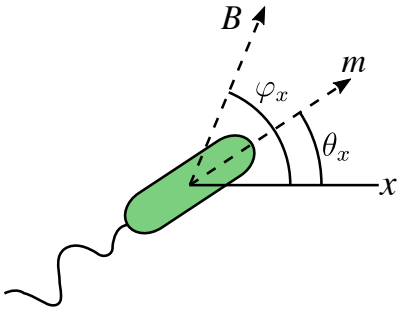

Figure 5: Bacterium at angle θ_x with magnetic field at angle φ_x.

$$x(t) = x(0) + \int_0^t v\cos(\theta_x(t))\mathrm{d}t \quad (33)$$

$$y(t) = y(0) + \int_0^t v\sin(\theta_x(t))\mathrm{d}t \quad (34)$$

$$\theta_x(t) = \theta_x(0) + \int_0^t \omega(t)\mathrm{d}t \quad (35)$$

$$\omega(t) = \frac{1}{f_\mathrm{b}}\left(\Gamma_\mathrm{mag}(t) + \Gamma_\mathrm{flag}(t)\right) \quad (36)$$

$$= \frac{mB}{f_\mathrm{b}}\sin(\varphi_x(t) - \theta_x(t)) + \frac{A_\mathrm{f}}{f_\mathrm{b}}\sin(\omega_\mathrm{f}t) \quad (37)$$

A linear, closed-form solution of the diameter of the trajectory of the U-turn in the case of an instantaneous field reversal and no flagellar torque is given by equation 29. This solution is not valid, however, in the case of slowly rotating fields. The experimental magnetic field is considered to rotate according to a constant-acceleration model with a total rotation period of 130 ms (see section 3.4). Simulations were carried out with time steps of 10 µs, which is comfortably fast and precise (decreasing this to 1 µs changes the results by approximately 0.01 %). Figure 6 shows several simulated trajectories subject to fields of various magnitudes, assuming nonzero flagellar torque and realistic MTB parameters.

Figure 7 shows the simulated v/D as a function of the field magnitude. It can be seen that during an instantaneous field reversal, the solution is nearly identical to the closed-form solution of equation 29. The difference is caused by the influence of flagellar torque. Introducing a field reversal time T_mag of 130 ms into a continuous-acceleration model significantly changes the profile, yielding a similar result for low fields, increasing at moderate fields, and saturating to a maximum value of 16.6 s^{-1}. B_opt is defined as the field magnitude at which v/D has the largest difference from the theoretical curve. Figure 8 shows, from simulations, that the optimal reversal time is inversely proportional to the magnetic field strength. For fields below B_opt, v/D can be considered linear with a maximum nonlinearity error of 2 %, independently of T_mag.

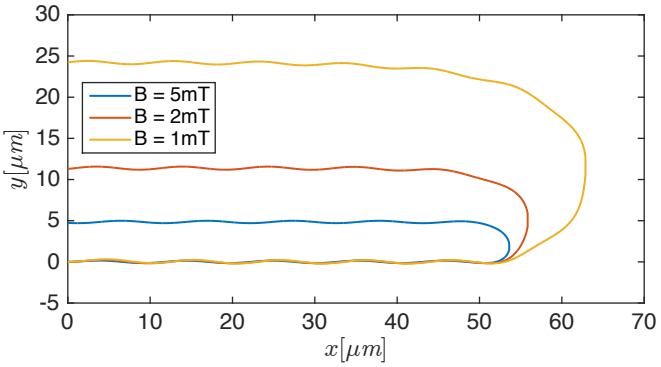

Figure 6: Simulated trajectories assuming flagellar torque and a non-instantaneously rotating field for several values of the magnetic field magnitude B. The time step of the simulation is 10 µs

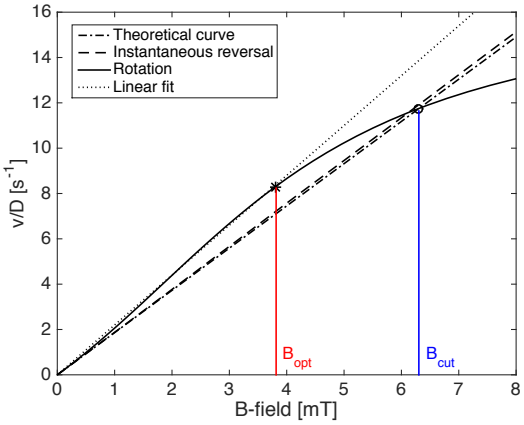

Figure 7: Simulated values of v/D for different rotation speeds of the magnetic field, with (red) and without (blue) and flagellar torque, compared with the linear model proposed by Erglis *et al.* [7] (dotted line).

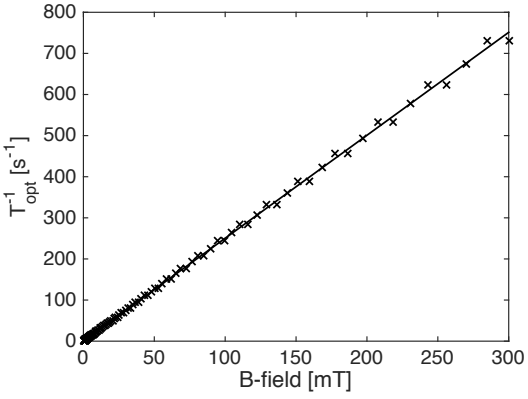

Figure 8: Simulated optimum reversal time of the magnetic field as a function of the field strength.

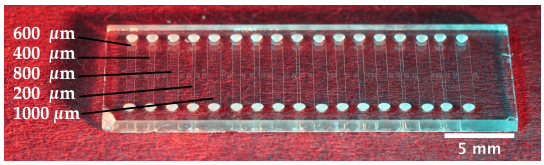

Figure 9: Top: A 5 µm deep microfluidic chip with various channel widths of 200, 400, 600, 800 and 1000 µm.

3. Experimental

3.1. Magnetotactic bacteria cultivation

A culture of *Magnetospirillum gryphiswaldense* was used for the magnetic moment study. The cultures were inoculated in MSGM medium ATCC 1653 according to with an oxygen concentration of 1 to 5 %. The bacteria were cultivated at 21 °C for 2 to 5 days for optimal chain growth [41]. The sampling was done using a magnetic "racetrack" separation, as described in [42].

3.2. Dynamic viscosity of growth medium

The kinematic viscosity of the freshly prepared growth medium was determined with an Ubbelohde viscometer with a capillary diameter of 0.63 ± 0.01 mm (Si Analytics 50110). The viscometer was calibrated with deionized water, assuming it has a kinematic viscosity of $0.98 \pm 0.01\,\mathrm{mm^2/s}$ at 21.0 ± 0.5 °C. At that temperature, the growth medium has a kinematic viscosity of $0.994 \pm 0.017\,\mathrm{mm^2/s}$. The density of the growth medium was $1.009 \pm 0.002\,\mathrm{g/cm^3}$, measured by weighing 1 ml of it on a balance. The dynamic viscosity of the growth medium is therefore 1.004 ± 0.019 mPas, which is, within measurement error, identical to water (1.002 mPas).

3.3. Microfluidic Chips

Microfluidic chips with a channel depth of 5 µm were constructed by lithography, HF etching in glass and subsequent thermal bonding. The fabrication process is identical to the one described in [43]. Figure 9 shows the resulting structures, consisting of straight channels with inlets on both sides. By means of these shallow channels, the MTBs are kept within the field of focus during microscopic observation, so as to prevent out-of-plane focus while tracking. The channel width was 200 µm or more, so that the area over which U-turns could be observed was only limited by the field of view of the microscope. The chips are positioned on a microcrope slide with the access holes down. A very thin layer of vasiline is applied between the chip and the microscope slide to obtain an tight seal so that oxygen cannot diffuse into the channel.

3.4. Magnetic Manipulation Setup

A schematic of the full setup, excluding the computer used for the acquisition of the images, is shown in figure 10. A permanent NdFeB magnet ($5 \times 5 \times 10$ mm, grade N42)

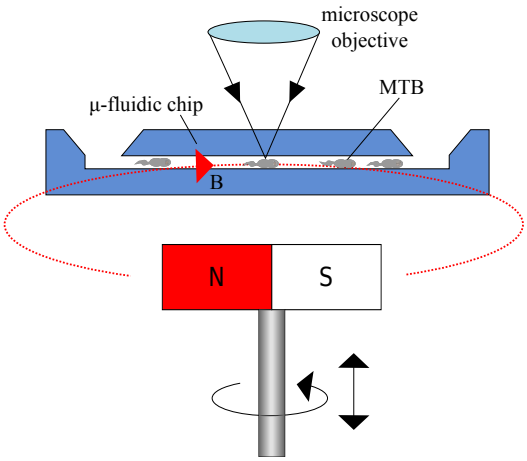

Figure 10: The setup used to measure the MTB U-turns. (a) Reflective microscope, (b) microfluidic chip and (c) a permanent magnet mounted on (d) a stepper motor.

is mounted on a stepper motor (Silverpak 17CE, Lin Engineering) below the microfluidic chip. The direction of the field can be adjusted with a precision of 51 200 steps for a full rotation, at a rotation time of 130 ms with a constant acceleration of $745\,\mathrm{rads^{-2}}$. The field strength is adjusted using a labjack, with a positioning accuracy of 0.5 mm.

The data acquisition was done by a Flea3 digital camera (1328×1048 at 100 fps, FL3-U3-13S2M-CS, Point Grey) mounted on a Zeiss Axiotron 2 microscope with a 20× objective.

During the experiments, a group of MTB was observed while periodically (every two seconds) rotating the magnetic field. This was recorded for field magnitudes ranging from 1 to 12 mT. Offline image processing techniques were used to track the bacteria and subtract their velocity and U-turn diameter.

Knowing the error in our measurements of the magnetic field is fundamental to determining the responsiveness of the MTB. Therefore we measured the magnetic fields at specific heights using a Hall meter (Metrolab THM1176). The results can be seen in figure 11.

The placement of the tip of the Hall meter was at the location of the microfluidic chip, assuming the field strength inside the chip's chamber equals that at the tip. It should be noted that the center of the magnet was aligned with the center of rotation of the motor, therefore the measurements were only done with a stationary magnet on top of an inactive motor. Errors in the estimation of the magnetic field strength due to misalignment of the magnetic center from our measurements therefore cannot be excluded.

The rotation profile of the motorized magnet was investigated by recording its motion by a digital camera at 120 fps and evaluating its time-dependent angle by manually drawing tangent lines. Figure 12 shows that the profile

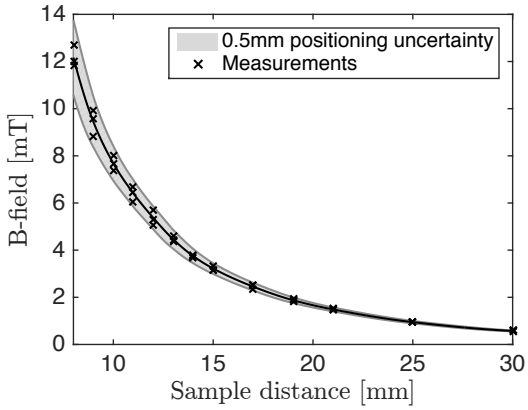

Figure 11: Magnetic field strength as a function of distance of the magnet to the microfluidic chip.

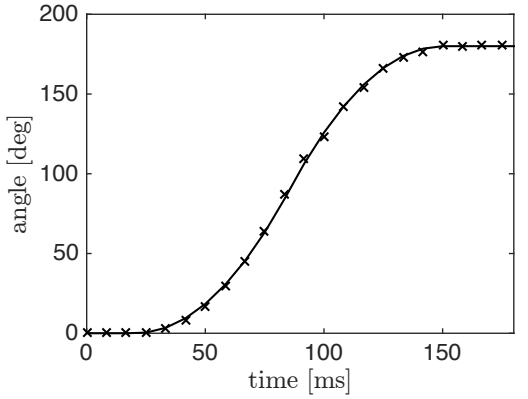

Figure 12: The measured angle of the motorized magnet accurately fits a constant-acceleration model with a total rotation period of 130 ms.

accurately fits a constant-acceleration model with an acceleration of 745 rads^{-2}, resulting in a total rotation time of 130 ms.

3.5. Macroscopic Drag Setup

Macro-scale drag measurements were performed using a Brookfield DV-III Ultra viscometer. During the experiment, we measured the torque required to rotate different centimeter sized models of bacteria and simple shapes in silicone oil (Figure 13). In order to keep the Reynolds number less than one, silicone oil of 5000 mPas (Calsil IP 5000 from Caldic, Belgium) was used as a medium to generate enough drag. Furthermore, the parts were rotated at speeds below 30 rpm. The models were realized by 3D printing. The designs can be found in the accompanying material.

3.6. Image Processing

The analysis of the data was done using in-house detection and tracking scripts written in MATLAB®. The

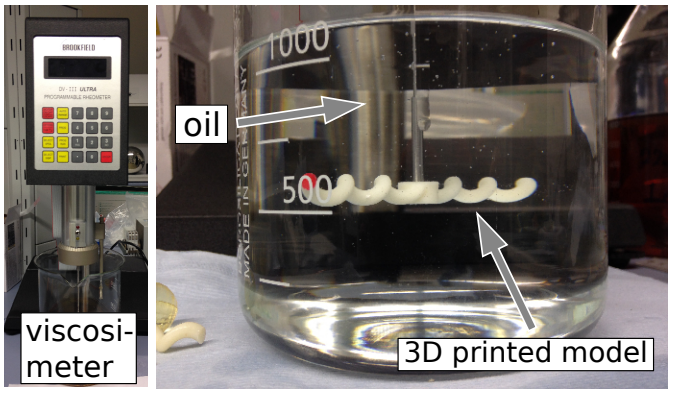

Figure 13: The viscometer setup used to measure the rotational drag of macroscopic spheroid and helical structures. 3D printed models were mounted on a shaft and rotated in a high viscosity silicone oil (5 Pas). A video of the experiment is available as additional material (DragMeasurements.mp4).

process is illustrated in figure 14. In the detection step, static objects and non-uniform illumination artefacts are removed by subtracting a background image constructed by averaging 30 frames spread along the video. High-frequency noise is reduced using a Gaussian lowpass filter. A binary image is then obtained using a thresholding operation, followed by selection on a minimum and maximum area size. The centers-of-mass of the remaining blobs are compared in subsequent frames, and woven to trajectories based on a nearest-neighbor search within a search radius 14. A sequence of preprocessing steps can be seen in figure 15. The software used is available under additional material.

Subsequently, the post-processing step involves the semi-automated selection of the MTB trajectories of interest for the purpose of analysis. The U-turn parameters of interest analyzed are the velocity v, the diameter D of the U-turn, and the time t. A typical result of the post-processing step can be seen in figure 16.

4. Results and discussions

The model developed in section 2 predicts the trajectories of MTB under a changing magnetic field: in particular, the average rate of rotation over a U-turn. To validate the model, the essential model parameters are determined in section 4.1, after which the average rate of rotation is measured and compared to theory in section 4.2.

4.1. Estimate of model parameters

The rate of rotation of an MTB under a rotating magnetic field is determined by the ratio between the rotational drag torque and the magnetic torque. Both will be discussed in the following, after which the average rate of rotation will be estimated.

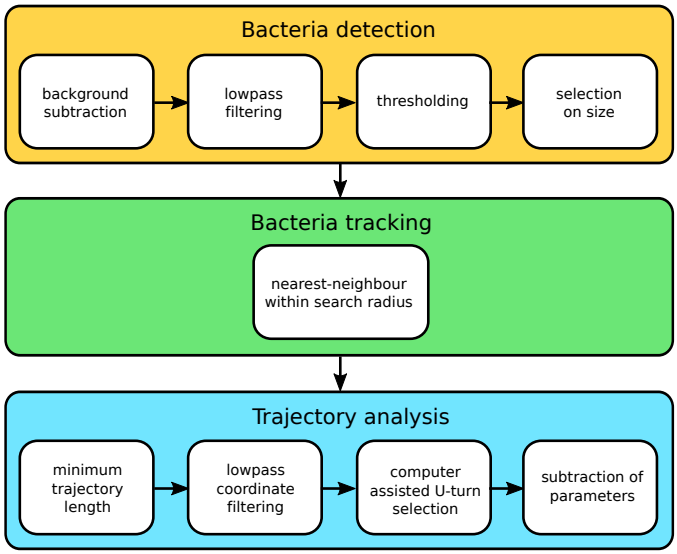

Figure 14: The process of bacteria detection, tracking, and subsequent analysis.

4.1.1. Estimate of rotational drag torque

To determine the rotational drag torque, the outer shape of the MTB was measured by both optical microscopy and scanning electron microscopy (SEM). The drag coefficient was estimated from a macroscale drag viscosity measurement.

Outer dimensions of the bacteria . The length L of the bacteria is measured from the same optical images as used for the trajectory analysis (figures 16). Scanning electron microscopy (SEM) would in principle give higher precision per bacterium, but due to the lower number of bacteria per image the estimate of the average length and distribution would have a higher error. Moreover, using the video footage ensures that the radius of curvature and the length of the bacteria are measured on the same bacterium.

A typical MSR-1 has a length of $5.0 \pm 0.2\,\mu\text{m}$. The length distribution is shown in Figure 18. These values agree with values reported in the literature [44, 45, 46].

The width W of the bacteria is too small to be determined by optical microscopy, and needs to be determined from SEM images, see figure 17. A typical bacterium has a width of $240 \pm 6\,\text{nm}$. The main issue with SEM images is whether a biological structure is still intact or perhaps collapsed due to dehydration, which might cause overestimation of the width. The latter might be as high as $\pi/2$ if the bacterial membrane has completely collapsed. Fortunately, the drag coefficient scales much more strongly with the length than with the width (equation 24). For a typical bacterium, the overestimation of the width by using SEM leads at most to an overestimation of the drag by 18 %.

Table 1 lists the values of the outer dimensions L and W, including the measurement error and standard deviation over the measured population.

Rotational Drag. From the outer dimensions of the bacteria, the rotational drag torque can be estimated. The bacterial shape correction factor, equation (25), was determined by macro-scale experiments with 3D printed models of an MTB in a viscosimeter using high viscosity silicone oil (see section 3.5). Figure 19 shows the measured torque as a function of the rotational speed for prolate spheroids and spiral shaped 3D printed bodies of two different lengths. The relation between the torque and the speed is linear, so we are clearly in the laminar flow regime. This is in agreement with an estimated Reynolds number of less than 0.3 for this experiment (equation 22). Independently of the size, the spiral shaped MTB models have a drag coefficient that is 1.64 ± 0.05 times higher (α_{BS}) than that of a spheroid of equal overall length and diameter.

Using the same experimental configuration, we can obtain an estimate of the effect of the channel walls on the rotational drag by changing the distance between the 3D printed model and the bottom of the container. Figure 20 shows the relative increase in drag when the spiral shape approaches the wall. This experiment was performed on a 5 cm long, 5 mm diameter spiral at 8 rpm. To visualise the increase, the reciprocal of the distance normalised to the length of the bacteria is used on the bottom horizontal axis. The normalised length is shown on the top axes. Note that when plotted in this way, the slope approaches unity at larger distances.

For an increase over 5 %, the model has to approach the wall at a distance smaller than $L/3$, where L is the length of the bacteria. For very long bacteria of 10 µm, this distance is already reached in the middle of the 5 µm high channel. Since there are two channel walls on either side at the same distance, we estimate that the additional drag for bacteria swimming in the centre of the channel is less than 15 %. If the spiral model approaches the wall, the drag rapidly increases. At $L/50$, the drag increases by 60 %. It is tempting to translate this effect to real MTB. It should be noted however that the 3D printed models are rigid and stationary, whereas the MTB are probably more flexible and mobile. Intuitively, one might expect a lower drag.

From the bacterial dimensions, we can estimate a mean rotational drag coefficient, f_{b}, of $67 \pm 7\,\text{zNms}$. Since the relation between the rotational drag and the bacterial dimensions is highly nonlinear, a Monte Carlo method was used to estimate the error and variation of f_{b}. For these calculations, the length of the bacteria was assumed to be Gaussian distributed with parameters as indicated in table 1. The code for the Monte Carlo calculation is available as additional material.

Due to the nonlinearity, the resulting distribution of f_{b} is asymmetric. So rather than the standard deviation, the 10 to 90 % cut-off values of the distribution are given in table 2). Most of the MTB are estimated to have a drag coefficient in the range of 30 to 120 zNms.

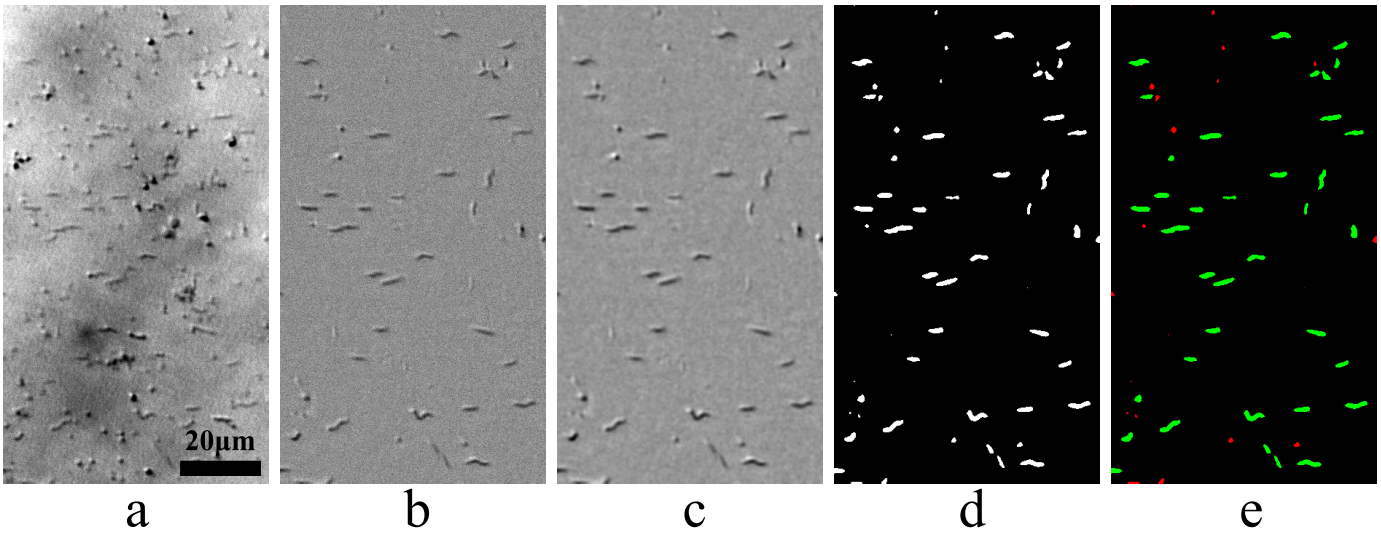

Figure 15: Pre-processing filter steps: (a) raw, (b) background subtraction, (c) low pass filtering, (d) thresholding resulting in a binary image, (e) size selectivity. A video is available as additional material

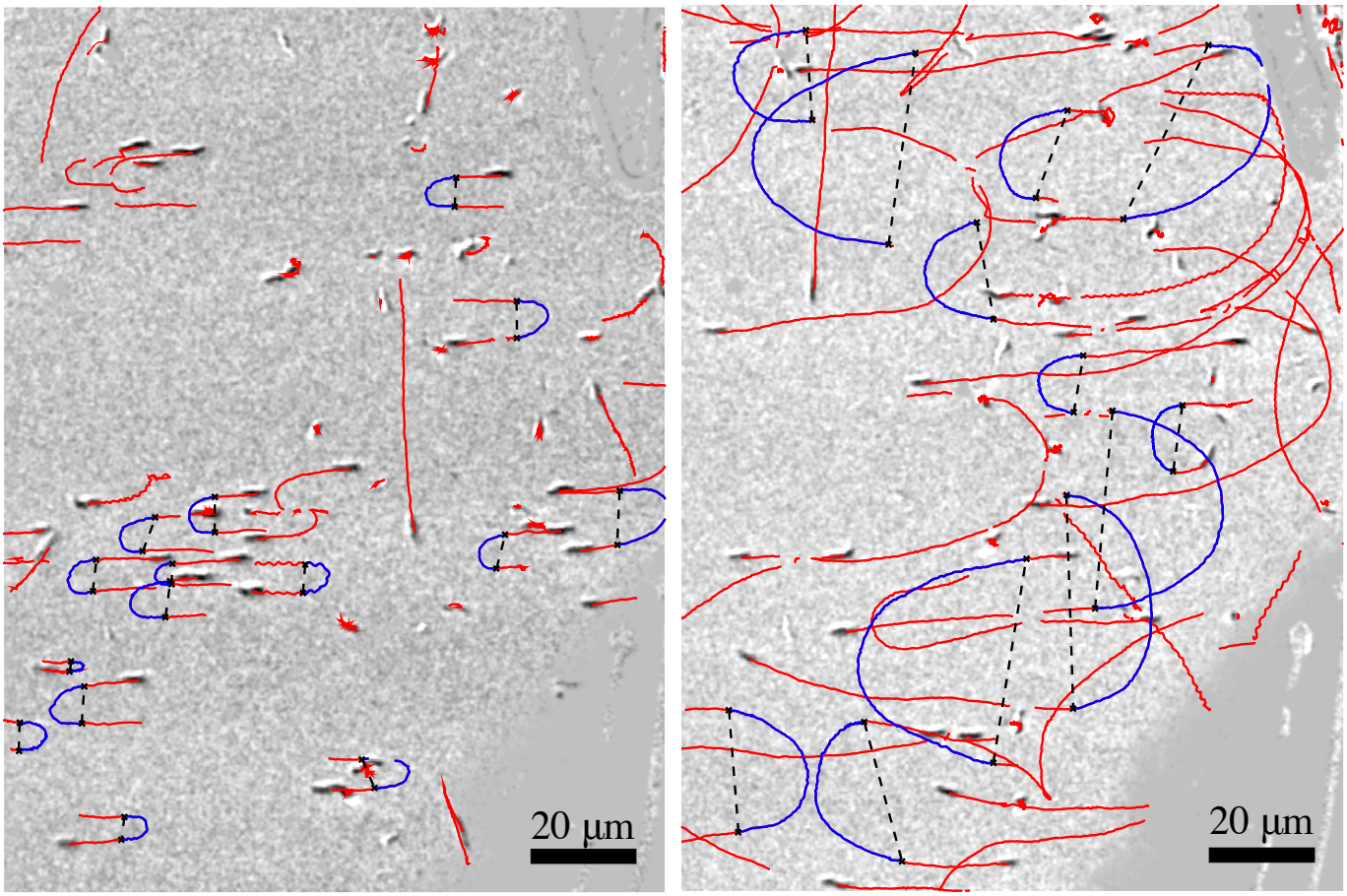

Figure 16: Trajectory during image post-processing at a magnetic field strength of 12.2 mT (left) and 1.5 mT (right). Selection procedure of analyzed U-turns, showing selected U-turns in blue and unanalyzed trajectories in red. The black dotted line connects two manually selected points of a given U-turn trajectory, from which the distance in the y-direction, or the U-turn diameter, is determined.

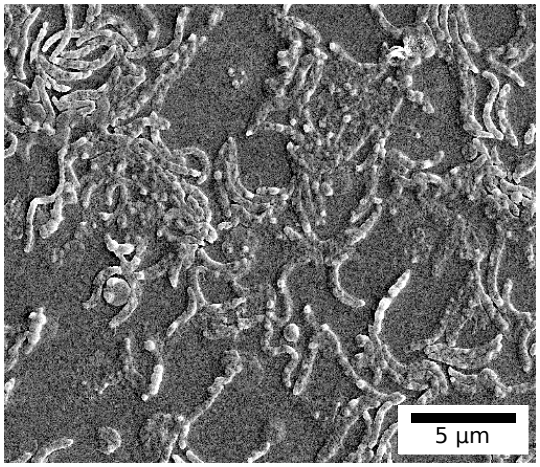

Figure 17: Scanning electron microscopy images of *Magnetospirillum gryphiswaldense*. Separated MTB were selected for width measurements.

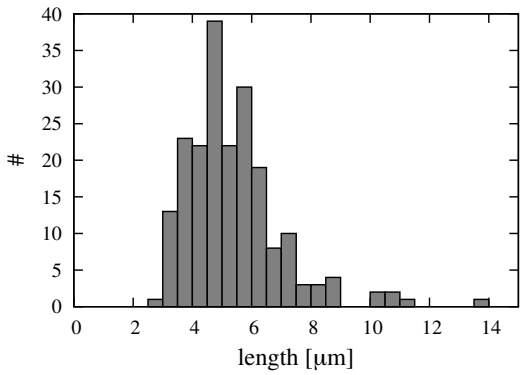

Figure 18: Number of magnetotactic bacteria (MTB) as a function of the length of the MTB as measured by optical microscopy.

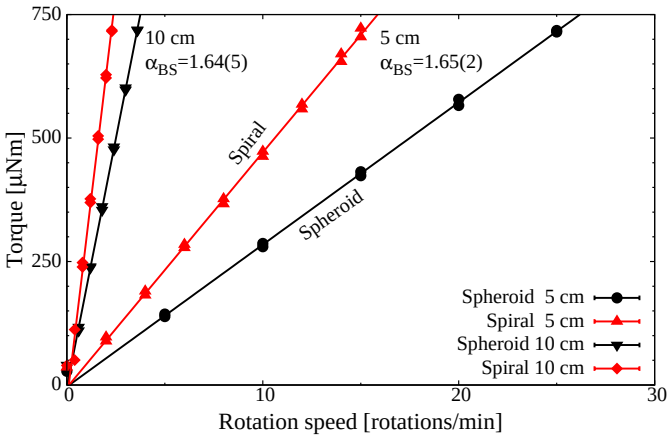

Figure 19: Rotational drag torque versus angular rotation speed of 3D printed prolate spheroids and MTB models of lengths 5 and 10 cm. The curves are linear, indicating that the flow around the objects is laminar. Irrespective of the length, the spiral shaped MTB model has a drag that is 1.64 ± 0.05 higher than a prolate spheroid of equal overall length and diameter.

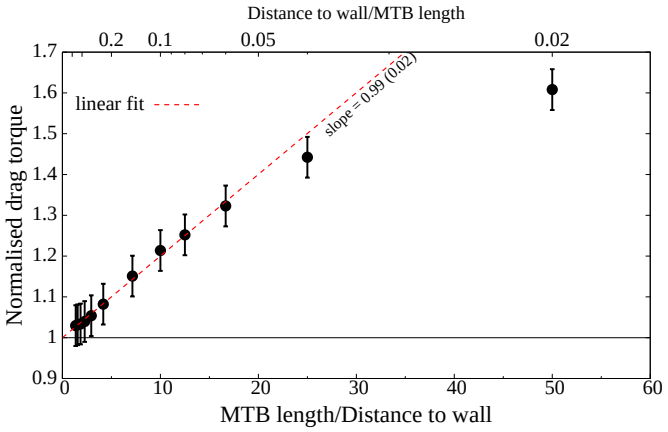

Figure 20: Increase in rotational drag as a function of the distance between the 3D printed spiral and the bottom of the container. The distance is normalized to the length of the bacteria (5 cm). The torque is normalized to the extrapolated value for infinite distance (displayed as "linear fit").

Table 1: Characteristics of magnetotactic bacteria. Length L and width W and amount n, radius r and center-to-center distance a of the crystals in the magnetosomes. The error indicated on the means is the standard error (standard deviation/square root of the total number of samples).

	L [µm]	W [nm]	n	r [nm]	a [nm]
mean	5.0 ± 0.2	240 ± 6	16 ± 2	20 ± 1	56 ± 1
stddev	1	28	6	5	8

Table 2: From the values of table 1, the drag coefficient f_b, demagnetisation factors ΔN, magnetic moment m, maximum magnetic torque Γ_max, and proportionality factor γ are estimated ($v/D = \gamma B$). The input parameters are assumed to obey a Gaussian distribution with standard deviations as in table 1. Using a Monte Carlo method, the standard error of the calculated parameters, and the 10 %–90 % cut-offs in the distribution, are calculated.

	f_b [zNms]	ΔN	m [fAm^2]	Γ_max [aNm]	γ_theory [rad/mTs]	γ_exp [rad/mTs]
mean	67 ± 7	0.10 ± 0.02	0.25 ± 0.05	7 ± 3	1.2 ± 0.3	0.74 ± 0.03
10 %	31	0.03	0.07	0.7	0.3	
90 %	124	0.27	0.57	41	3.6	

4.1.2. Estimate of magnetic torque

Figure 21 shows typical transmission electron microscopy images (TEM) of magnetosome chains. From these images, we obtain the magnetosome count n, radius r, and center-to-center distance a, which are listed as well in table 1. These values agree with those reported in the literature [47, 46] and lie within the range of single-domain magnets [48]. We have found no significant relation between the inter-magnetosome distance and the chain length, see figure 22.

From these values the demagnetisation factor ΔN, the magnetic moment m, and the maximum torque Γ_max are calculated using the model from section 2.1, and tabulated in table 2. Again, the standard deviations of the values and the 10%- and 90 % cut-off values are determined from Monte Carlo simulations. The estimated value of the magnetic moment is in agreement with values reported in literature (0.1-0.4 Am^2) [49].

4.1.3. Average rate of rotation

From the drag coefficient f_b and the maximum torque Γ_max, the ratio γ between the average rate of rotation and the magnetic field strength can be obtained using equation 30. This value is listed as γ_theory in table 2, and has a convenient value of approximately 1 rad/mTs. So in the earth's magnetic field (0.04 mT), the rate of rotation of an MSR-1 is approxmately 0.04 rad/s. A U-turn will take at least 78 s.

4.1.4. Average Velocity

The MTBs' velocity was determined from the full set of 174 analyzed bacteria trajectories. This set has a mean velocity of 49.5 ± 0.7 µm/s with a standard deviation σ of 8.6 µm/s (figure 23). Using the value for the average rate of rotation γ of approximately 1 rad/mTs, this speed leads to a U-turn in the earth's magnetic field of about 1 mm (equation 30).

The average velocity of the bacteria is close to the value reported by Popp for *Magnetospirillum gryphiswaldense* in an oxygen gradient free environment (42 ± 4 µm/s [50]), and much higher than that reported by Lefevre for bacteria in the vicinity of an oxic-anoxic zone (13 to 23 µm/s [51]). This suggests that there is no oxygen gradient, which is in agreement with the fact that we seal the chip before observation.

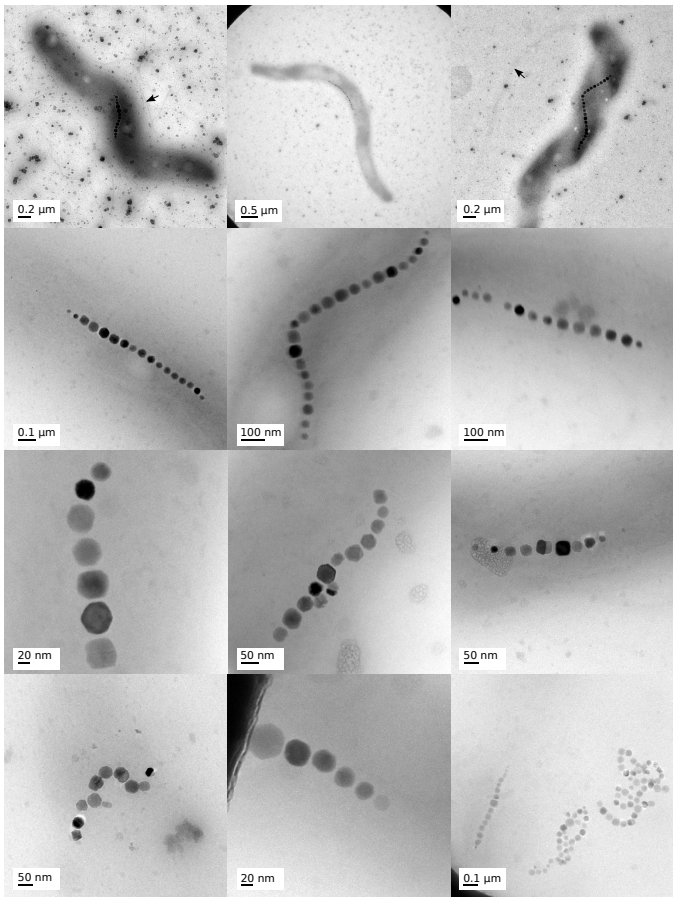

Figure 21: Transmission electron micrographs of MSR-1, magnetosomes and chains. The top row shows typical full scale bacteria, where black arrows indicate the flagella. Compared to the second row, the third row shows shorter chains with a higher variety in size distribution of magnetic nanoparticles due to an immaturity of the chain [5]. The bottom row shows irregular chains and overlapping groups of expelled chains due to the formation of aggregates, making it hard or impossible to distinguish individual chains.

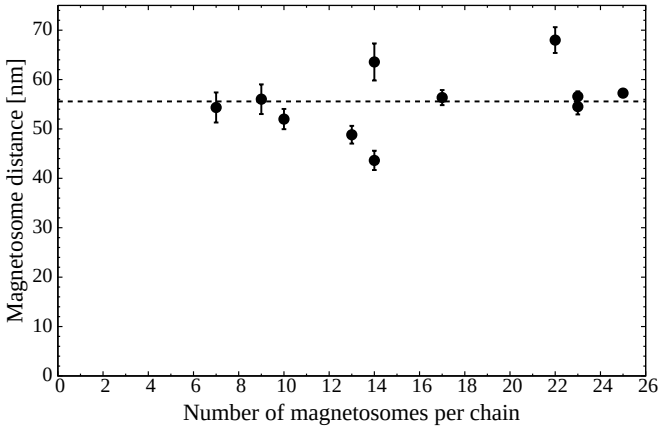

Figure 22: Distance between magnetite particles as a function of the number of particles in the chain. The mean of the entire sample group is indicated with a dashed line at 56 ± 1 nm. Vertical error bars represent the standard error of each individual chain.

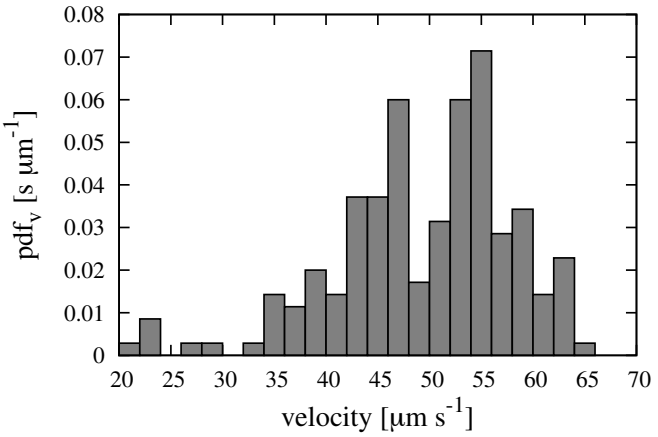

Figure 23: Probability density function for the MTB velocity distribution for 174 observed MTB.

Depending on the choice of binning, one might recognise a dip in the velocity distribution. Similar dips have been found in previous research, which were attributed to different swimming modes [25]. There might as well be possible wall-effects on bacteria caused by the restricted space in the microfluidic chip [52].

The measured velocity during U-turns as a function of the magnetic field strength is shown in figure 24. The vertical error bars display the standard error of the velocity within the group. The size of the sample group is depicted above the vertical error bars. For every sample group containing less than ten bacteria, the standard deviation of the entire population was used instead. The error in the magnetic field is due to positioning error, as described in section 3.4.

On the scale of the graph, the deviation from the mean velocity is seemingly large, especially below 2 mT. This

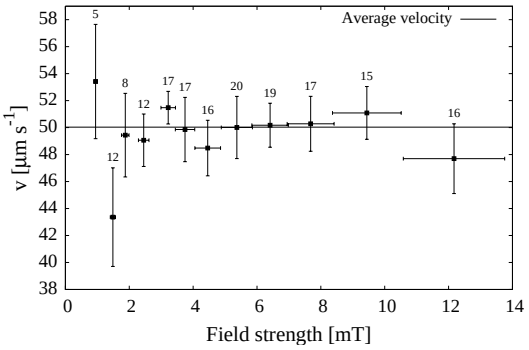

Figure 24: Average MTB velocity as function of the applied magnetic field. The vertical error bars indicate the standard error calculated from the number of bacteria indicated above the error bar.

deviation is however not statistically significant. The reduced χ^2 of the fit to the field-independent model is very close to unity (0.67), with a high Q-value of 0.77 (the probability that χ^2 would even exceed that value by chance, see Press *et al.*, chapter 15 [53]). Within the standard errors obtained in this measurement, and for the range of field values applied, we can conclude that the velocity of the MTB is independent of the applied magnetic field, as expected.

4.2. Trajectories

The diameter D of the U-turn was measured from the trajectories as in figure 16. From these values and the measured velocity v for each individual bacterium, the average rate of rotation v/D can be calculated. Figure 25 shows this average rate of rotation as a function of the applied magnetic field, B. The error bars are defined as in figure 24.

The data points are fitted to the U-turn trajectory model simulations of section 2.2. The fit is shown as a solid black line, with the proportionality factor γ_{exp} equal to 0.74 ± 0.03 rad/mTs. The reduced χ^2 of the fit is (2.88), and the Q-value (0.000 86)

Figure 25 shows that the observed average rate of rotation in low fields is higher than the model fit in comparison with the measurement error. We neglected the effect of the (earth's) magnetic background field. As discussed before, at this field strength, however, the average rate of rotation is on the order of 40 mrad/s and the corresponding diameter of a U-turn is on the order of 1 mm. The background field can therefore not be the cause of any deviation at low field strengths. Tracking during the pre-processing step under low fields leads to an overlap between the trajectories, which affect the post-processing step. Due to the manual selection in the post-processing, illustrated in figure 16, the preference for uninterrupted and often shorter trajectories may have led (for lower fields) to a selection bias to smaller curvatures. The deviation from the linear fit below 2 mT could therefore be attributed to human bias ("cherry picking").

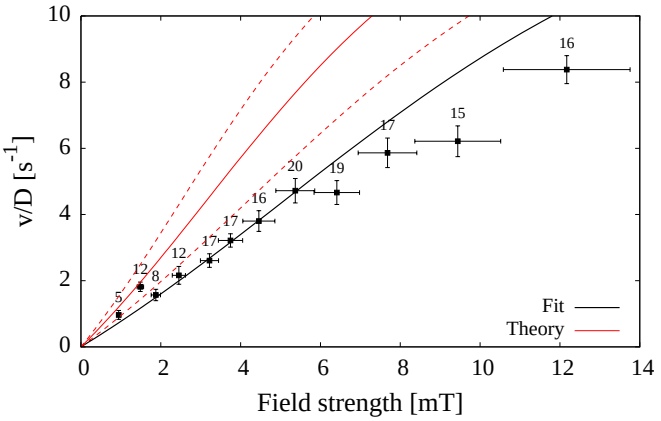

Figure 25: The average rate of rotation, v/D, as a function of the applied magnetic field, B. Vertical error bars display the standard error calculated for the number of MTB denoted above the error bars. For remaining sample groups, containing less than 10 bacteria samples, the standard deviation of the entire population is used instead. The black solid line is the fit of the model to the measured data, resulting in $\gamma_{\text{exp}} = 0.74 \pm 0.03\,\text{rad/mTs}$. The solid red line is the model prediction, using the γ_{theory} derived from the bacteria and magnetosome dimensions, with the dotted red lines indicating the error on the estimate ($1.2 \pm 0.3\,\text{rad/mTs}$).

If we neglect trajectories below 2 mT for this reason, the fits improve (drastically) for both the velocity and average rate of rotation. Fitting datapoints over the range of 2 to 12 mT (eight degrees of freedom) decreases the reduced χ^2 of the velocity from 0.67 to 0.42. Furthermore, the Q-value of 0.77 is increased to 0.91, a slight increase in likelihood that our datapoints fall within the limits of the model.

Similarly, the reduced χ^2 of the average rate of rotation is lowered from 2.88 to 1.03 and the Q-value from 0.000 86 to 0.41, a drastic change in likelihood of the fit. We therefore assume that these results validate the model with the exclusion of outliers below 2 mT.

At high fields, the observed average rate of rotation seems to be on the low side, although within the error bounds. For the high field range, the diameter of a U-turn is on the order of 5 µm and reversal times are on the order of 100 ms. The resolving power of our setup of 180 nm/pixel and time resolution of 100 frames/s are sufficient to capture these events, so cannot explain the apparent deviation.

A second option is that the weakest bacteria reach the saturation torque value. As can been seen in figure 4, this would only be the case for about 10 to 20 % of the population, and the difference with the linear model would only be about 20 %. The combined effect would therefore be less than 2 %, which is too low to explain the reduction at higher field. To solve this issue experiments as a fuction of the applied field on an individual bacterium, preferably at higher field values, will be required. Unfortunately, this is outside the range of possiblities of our experimental setup.

5. Discussion

Figure 25 shows in red the prediction of the model using the proportionality factor determined from observations of the MTB (the outer dimensions by optical microsopy and SEM, the magnetosome by TEM). For the fields up to approximately 5 mT the relationships is linear. At higher fields the average slightly decreases, but the effect is smaller than the standard error on our measurements. Our experiments confirm that the linear model that has been used up to now in the research on magnetotactic bacteria is a good approximation for fields below 10 mT.

The proportionality factor in the linear regime is $\gamma_{\text{theory}} = 1.2 \pm 0.3\,\text{rad/mTs}$. The predicted proportionaliy factor is clearly higher than measured. This is either because we overestimated the magnetic moment or underestimated the rotational drag coeffient. The latter seems more likely. Even though we include the spiral shape of the bacteria, we still neglected the influence of the flagella. A coarse estimate using a rigid cylinder model for the flagellum shows that a flagellum could indeed cause this type of increase in drag. Since we lack information on the flexibility of the flagellum, we cannot quantify the additional drag. Secondly, we ignored the finite height of the microfluidic channel. As was shown by the macroscale experiments, the additional drag increases rapidly if a bacterium approaches within a few hundred nanometers of the wall. Since we do not have information about the distance, again quantification is difficult.

Given the above considerations, we are confident that over the observed field range, the MTB trajectories are in fair agreement with our model.

6. Conclusion

We studied the response of the magnetotactic bacteria *Magnetospirillum gryphiswaldense* to rotation of an external magnetic field B, ranging in amplitude from 1 mT up to 12 mT.

Our magnetic model shows that the torque on the MTB is linear in the applied field up to 10 mT, after which the torque starts to saturate for an increasing part of the population.

Our theoretical analysis of bacterial trajectories shows that the bacteria perform a U-turn under 180° rotation of the external field, but not at a constant angular velocity. The diameter, D, of the U-turn increases with an increase in the velocity v of the bacteria. The average rate of rotation, v/D, for an instantaneously reversing field is linear within 2 % in the applied field up to 12 mT.

If the applied field is rotated over 180° in a finite time, the average rate of rotation is higher at low field values than it was for an instantaneous reversal. Given a field rotation time, an optimum field value exist at which the

rate of rotation is approximately 18 % higher than for instantaneous reversal. This optimum field value is inversely proportional to the field rotation time.

The rotational drag coefficient for an MTB was estimated from drag rotation experiments in a highly viscous fluid, using a macroscale 3D printed MTB model. The spiral shape of the body of an MTB has a 64 ± 5 % higher drag than a spheroid with equal length and diameter, which has been the default model in the literature up to now. Furthermore, the added drag from the channel wall was found to be negligible for an MTB in the center between the walls (less than 10 %), but to increase rapidly when the MTB approaches to within a few hundred nanometers of one of the walls.

From microscope observations, we conclude that the MTB velocity during a U-turn is independent of the applied field. The population of MTB has a non-Gaussian distributed velocity, with an average of $49.5 \pm 0.7\,\mu m/s$ and a standard deviation of $8.6\,\mu m/s$. As predicted by our model, the average rate of rotation is linear in the external magnetic field within the measured range of 1 to 12 mT. The proportionality factor $\gamma = v/DB$ equals $0.74 \pm 0.03\,rad/mTs$. The predicted theoretical value is $1.2 \pm 0.3\,rad/mTs$, which is based on measurements of the parameters needed for the model, such as the size of the bacteria and their magnetosomes from optical microscopy, SEM, and TEM images. The number of parameters and their nonlinear relation with the proportionality factor causes the relatively large error in the estimate.

These findings finally prove that the generally accepted linear model for the response of MTB to external magnetic fields is correct within the errors caused by the estimation of the model parameters if the field values are below 12 mT. At higher values, torque saturation will occur.

This result is of importance to the control engineering community. The knowledge of the relation between the angular velocity and the field strength (γ) can be used to design energy efficient control algorithms that prevent the use of excessive field strengths. Furthermore, a better understanding of the magnetic behavior will lead to more accurate predictions of the dynamic response of MTB for potential applications in micro-surgery, as drug carriers, or for drug delivery.

Acknowledgments

The authors wish to thank Matthias Altmeyer of KIST Europe for assistance in cultivating the bacteria, Lars Zondervan of the University of Twente for calculations of demagnetization factors, Jorg Schmauch of the Institute for New Materials in Saarbrücken, Germany, for TEM imaging, and Carsten Brill of KIST Europe for SEM imaging.

[1] R. P. Blakemore, D. Maratea, R. S. Wolfe, Isolation and pure culture of a freshwater magnetic spirillum in chemically defined medium., Journal of Bacteriology 140 (2) (1979) 720–729. arXiv:http://jb.asm.org/content/140/2/720.full.pdf+html.

[2] A. Komeili, H. Vali, T. Beveridge, D. Newman, Magnetosome vesicles are present before magnetite formation, and mama is required for their activation, Proceedings of the National Academy of Sciences of the United States of America 101 (11) (2004) 3839–3844. doi:10.1073/pnas.0400391101.

[3] U. Lins, M. McCartney, M. Farina, R. Frankel, P. Buseck, Habits of magnetosome crystals in coccoid magnetotactic bacteria, Applied and Environmental Microbiology 71 (8) (2005) 4902–4905. doi:10.1128/AEM.71.8.4902-4905.2005.

[4] J. Baumgartner, D. Faivre, Magnetite biomineralization in bacteria, in: W. E. G. Muller (Ed.), Molecular Biomineralization, Vol. 52 of Progress in Molecular and Subcellular Biology, Springer Berlin, 2011, pp. 3–27. doi:10.1007/978-3-642-21230-7_1.

[5] R. Uebe, D. Schüler, Magnetosome biogenesis in magnetotactic bacteria, Nature Reviews Microbiology 14 (10) (2016) 621–637. doi:10.1038/nrmicro.2016.99.

[6] Y. Gorby, T. Beveridge, R. Blakemore, Characterization of the bacterial magnetosome membrane., Journal of Bacteriology 170 (2) (1988) 834–841.

[7] K. Erglis, Q. Wen, V. Ose, A. Zeltins, A. Sharipo, P. A. Janmey, A. Cebers, Dynamics of magnetotactic bacteria in a rotating magnetic field, Biophysical Journal 93 (4) (2007) 1402–1412. doi:10.1529/biophysj.107.107474.

[8] J. Kirschvink, M. Walker, C. Diebel, Magnetite-based magnetoreception, Current Opinion in Neurobiology 11 (4) (2001) 462–467. doi:10.1016/S0959-4388(00)00235-X.

[9] R. Frankel, D. Bazylinski, M. Johnson, B. Taylor, Magneto-aerotaxis in marine coccoid bacteria, Biophysical Journal 73 (2) (1997) 994–1000.

[10] S. Maus, S. Macmillan, S. McLean, B. Hamilton, A. Thomson, M. Nair, C. Rollins, The us/uk world magnetic model for 2010-2015, Tech. rep., British Geological Survey (December 2010).

[11] D. Esquivel, H. Lins de Barros, Motion of magnetotactic microorganisms, Journal of Experimental Biology VOL. 121 (1986) 153–163.

[12] A. Bahaj, P. James, Characterisation of magnetotactic bacteria using image processing techniques, IEEE Transactions on Magnetics 29 (6) (1993) 3358–3360. doi:10.1109/20.281175.

[13] A. Bahaj, P. James, F. Moeschler, An alternative method for the estimation of the magnetic moment of non-spherical magnetotactic bacteria, IEEE Transactions on Magnetics 32 (5 PART 2) (1996) 5133–5135. doi:10.1109/20.539514.

[14] N. van Kampen, The turning of magnetotactic bacteria, Journal of Statistical Physics 80 (1-2) (1995) 23–33. doi:10.1007/BF02178351.

[15] A. Cebers, Diffusion of magnetotactic bacterium in rotating magnetic field, Journal of Magnetism and Magnetic Materials 323 (3-4) (2011) 279–282. doi:10.1016/j.jmmm.2010.09.017.

[16] A. Menciassi, M. Quirini, P. Dario, Microrobotics for future gastrointestinal endoscopy, Minimally Invasive Therapy & Allied Technologies 16 (2007) 91–100.

[17] J. J. Abbott, M. Cosentino Lagomarsino, L. Zhang, L. Dong, B. J. Nelson, How should microrobots swim?, The International Journal of Robotics ResearcharXiv:http://ijr.sagepub.com/content/early/2009/07/21/0278364909341658.full.pdf+html, doi:10.1177/0278364909341658.

[18] H. Nelson, D. Sargent, H. Wieand, J. Fleshman, M. Anvari, S. Stryker, R. Beart Jr., M. Hellinger, R. Flanagan Jr., W. Peters, D. Ota, A comparison of laparoscopically assisted and open colectomy for colon cancer, New England Journal of Medicine 350 (20) (2004) 2050–2059+2114. doi:10.1056/NEJMoa032651.

[19] M. Abayazid, R. J. Roesthuis, R. Reilink, S. Misra, Integrating deflection models and image feedback for real-time flexible needle steering, IEEE transactions on robotics 29 (2) (2013) 542–553.

[20] O. Felfoul, M. Mohammadi, S. b. Taherkhani, D. De Lanauze, Y. Zhong Xu, D. Loghin, S. d. Essa, S. Jancik, D. Houle, M. Lafleur, L. Gaboury, M. f. Tabrizian, N. Kaou, M. Atkin, T. Vuong, G. Batist, N. Beauchemin, D. Radzioch, S. Martel, Magneto-aerotactic bacteria deliver drug-containing nano-

liposomes to tumour hypoxic regions, Nature Nanotechnology 11 (11) (2016) 941–947. doi:10.1038/nnano.2016.137.

[21] J. Dankelman, J. van den Dobbelsteen, P. Breedveld, Current technology on minimally invasive surgery and interventional techniques, in: Instrumentation Control and Automation (ICA), 2011 2nd International Conference on, 2011, pp. 12–15. doi:10.1109/ICA.2011.6130118.

[22] B. Nelson, I. Kaliakatsos, J. Abbott, Microrobots for minimally invasive medicine, Annual Review of Biomedical Engineering 12 (2010) 55–85. doi:10.1146/annurev-bioeng-010510-103409.

[23] I. S. M. Khalil, M. P. Pichel, L. Abelmann, S. Misra, Closed-loop control of magnetotactic bacteria, The International Journal of Robotics Research 32 (6) (2013) 637–649. doi:10.1177/0278364913479412.

[24] C. Yang, C. Chen, Q. Ma, L. Wu, T. Song, Dynamic model and motion mechanism of magnetotactic bacteria with two lateral flagellar bundles, Journal of Bionic Engineering 9 (2) (2012) 200–210. doi:10.1016/S1672-6529(11)60108-X.

[25] M. Reufer, R. Besseling, J. Schwarz-Linek, V. Martinez, A. Morozov, J. Arlt, D. b. Trubitsyn, F. Ward, W. Poon, Switching of swimming modes in magnetospirillium gryphiswaldense, Biophysical Journal 106 (1) (2014) 37–46. doi:10.1016/j.bpj.2013.10.038.

[26] P. Smid, V. Shcherbakov, N. Petersen, Microscopic observation of magnetic bacteria in the magnetic field of a rotating permanent magnet, Review of Scientific Instruments 86 (9). doi:10.1063/1.4929331.

[27] S. Martel, M. Mohammadi, O. Felfoul, Z. Lu, P. Pouponneau, Flagellated magnetotactic bacteria as controlled mri-trackable propulsion and steering systems for medical nanorobots operating in the human microvasculature, International Journal of Robotics Research 28 (4) (2009) 571–582. doi:10.1177/0278364908100924.

[28] S. Martel, M. Mohammadi, Using a swarm of self-propelled natural microrobots in the form of flagellated bacteria to perform complex micro-assembly tasks, Proceedings - IEEE International Conference on Robotics and Automation (2010) 500–505doi:10.1109/ROBOT.2010.5509752.

[29] D. De Lanauze, O. Felfoul, J.-P. Turcot, M. Mohammadi, S. Martel, Three-dimensional remote aggregation and steering of magnetotactic bacteria microrobots for drug delivery applications, International Journal of Robotics Research 33 (3) (2014) 359–374. doi:10.1177/0278364913500543.

[30] H. Hassan, M. Pichel, T. Hageman, L. Abelmann, I. S. M. Khalil, Influence of the magnetic field on the two-dimensional control of magnetospirillum gryphiswaldense strain msr-1, in: Proceedings of the IEEE International Conference on Intelligent Robots and Systems (IROS), Daejeon, Korea, 2016, pp. 5119–5124.

[31] A. Hubert, R. Schäfer, Magnetic domains: the analysis of magnetic microstructures, Springer-Verlag, Berlin, Heidelberg, New-York, 1998.

[32] I. Jacobs, C. Bean, An approach to elongated fine-particle magnets, Physical Review 100 (4) (1955) 1060–1067. doi:10.1103/PhysRev.100.1060.

[33] A. Witt, K. Fabian, U. Bleil, Three-dimensional micromagnetic calculations for naturally shaped magnetite: Octahedra and magnetosomes, Earth and Planetary Science Letters 233 (3-4) (2005) 311–324. doi:10.1016/j.epsl.2005.01.043.

[34] D. J. Griffiths, Introduction to electrodynamics, 3rd Edition, Prentice Hall, Upper Saddle River, New Jersey, 1999.

[35] B.-K. Hu, Averages of static electric and magnetic fields over a spherical region: A derivation based on the mean-value theorem, American Journal of Physics 68 (11) (2000) 1058–1060.

[36] B.-K. Hu, Averages of static electric and magnetic fields over a spherical region: A derivation based on the mean-value theorem, arXiv:physics/0002021 [physics.ed-ph].

[37] M. Hanzlik, M. Winklhofer, N. Petersen, Spatial arrangement of chains of magnetosomes in magnetotactic bacteria, Earth and Planetary Science Letters 145 (1-4) (1996) 125–134.

[38] S. Dennis, S. Singh, D. Ingham, Steady flow due to a rotating sphere at low and moderate reynolds numbers., Journal of Fluid Mechanics 101 (pt 2) (1980) 257–279.

[39] J. Dote, D. Kivelson, Hydrodynamic rotational friction coefficients for nonspheroidal particles, Journal of Physical Chemistry 87 (20) (1983) 3889–3893.

[40] H. C. Berg, Random Walks in Biology, Princeton University Press, 1993.

[41] E. Katzmann, M. Eibauer, W. Lin, Y. Pan, J. Plitzko, D. Schuler, Analysis of magnetosome chains in magnetotactic bacteria by magnetic measurements and automated image analysis of electron micrographs, Applied and Environmental Microbiology 79 (24) (2013) 7755–7762. doi:10.1128/AEM.02143-13.

[42] R. S. Wolfe, R. K. Thauer, N. Pfenning, A 'capillary racetrack' method for isolation of magnetotactic bacteria, FEMS Microbiology Ecology 45 (1987) 31–35.

[43] J. K. Park, C. D. M. Campos, P. Neuzil, L. Abelmann, R. M. Guijt, A. Manz, Direct coupling of a free-flow isotachophoresis (ffitp) device with electrospray ionization mass spectrometry (esi-ms), Lab Chip 15 (2015) 3495–3502. doi:10.1039/C5LC00523J.

[44] K. Schleifer, D. Schuler, S. Spring, M. Weizenegger, R. Amann, W. Ludwig, M. Kohler, The genus magnetospirillum gen. nov. description of magnetospirillum gryphiswaldense sp. nov. and transfer of aquaspirillum magnetotacticum to magnetospirillum magnetotacticum comb. nov., Systematic and Applied Microbiology 14 (4) (1991) 379–385.

[45] D. Bazylinski, R. Frankel, Magnetosome formation in prokaryotes, Nature Reviews Microbiology 2 (3) (2004) 217–230. doi:10.1038/nrmicro842.

[46] D. Faivre, A. Fischer, I. Garcia-Rubio, G. Mastrogiacomo, A. Gehring, Development of cellular magnetic dipoles in magnetotactic bacteria, Biophysical Journal 99 (4) (2010) 1268–1273. doi:10.1016/j.bpj.2010.05.034.

[47] M. Pósfai, T. Kasama, R. E. Dunin-Borkowski, Characterization of bacterial magnetic nanostructures using high-resolution transmission electron microscopy and off-axis electron holography, in: D. Schüler (Ed.), Magnetoreception and Magnetosomes in Bacteria, Springer-Verlag, Berlin, Berlin, Heidelberg, 2007, pp. 197–225. doi:10.1007/7171_044.

[48] D. Faivre, Formation of magnetic nanoparticle chains in bacterial systems, MRS Bulletin 40 (6) (2015) 509–515. doi:10.1557/mrs.2015.99.

[49] R. Nadkarni, S. Barkley, C. Fradin, A comparison of methods to measure the magnetic moment of magnetotactic bacteria through analysis of their trajectories in external magnetic fields, PLoS ONE 8 (12). doi:10.1371/journal.pone.0082064.

[50] F. Popp, J. Armitage, D. Schüler, Polarity of bacterial magnetotaxis is controlled by aerotaxis through a common sensory pathway, Nature Communications 5. doi:10.1038/ncomms6398.

[51] C. Lefèvre, M. Bennet, L. Landau, P. Vach, D. Pignol, D. Bazylinski, R. Frankel, S. Klumpp, D. Faivre, Diversity of magneto-aerotactic behaviors and oxygen sensing mechanisms in cultured magnetotactic bacteria, Biophysical Journal 107 (2) (2014) 527–538. doi:10.1016/j.bpj.2014.05.043.

[52] Y. Magariyama, M. Ichiba, K. Nakata, K. Baba, T. Ohtani, S. Kudo, T. Goto, Difference in bacterial motion between forward and backward swimming caused by the wall effect, Biophysical Journal 88 (5) (2005) 3648–3658. doi:10.1529/biophysj.104.054049.

[53] W. H. Press, S. A. Teukolsky, W. T. Vetterling, B. P. Flannery, Numerical Recipes in C (2nd Ed.): The Art of Scientific Computing, Cambridge University Press, 1992.